DOI: 10.1002/ejic.201100364

Crystal Structure, Charge Transport, and Magnetic Properties of $MnSb_2Se_4$

Honore Djieutedjeu,[a,b] Julien P. A. Makongo,[a] Aurelian Rotaru,[a] Andriy Palasyuk,[c] Nathan J. Takas,[a] Xiaoyuan Zhou,[d] Kulugammana G. S. Ranmohotti,[a] Leonard Spinu,[a] Ctirad Uher,[d] and Pierre F. P. Poudeu*[a,b][‡]

Dedicated to Professor John D. Corbett on the occasion of his 85th birthday

Keywords: Manganese / Antimony / Selenium / Semiconductors / Magnetic properties / Thermoelectricity

A single phase of $MnSb_2Se_4$ was synthesized by combining high-purity elements at 773 K. Single-crystal X-ray diffraction revealed that $MnSb_2Se_4$ is isostructural with $FeSb_2Se_4$ crystallizing in the monoclinic space group $C2/m$ with a = 13.076(3) Å, b = 3.965(2) Å, c = 15.236(4) Å, β = 115.1(2)°, Z = 4. $MnSb_2Se_4$ melts congruently at 790 K and is thermally stable up to 1000 K. Electronic band structure calculations, infrared diffuse reflectance spectroscopy, and low-temperature electronic transport data indicate that $MnSb_2Se_4$ is a narrow-bandgap p-type semiconductor with an energy bandgap of approximately 0.31 eV and exhibits a sharp increase in the resistivity near 230 K. A large Seebeck coefficient (S = +945 μV K^{-1}), high electrical resistivity ($\rho \approx 9\ \Omega$m), and low thermal conductivity (κ = 1.4 W m^{-1} K^{-1}) were observed at 300 K. Direct current (DC) magnetic-susceptibility measurements indicated that $MnSb_2Se_4$ is paramagnetic at 300 K and undergoes an order/disorder antiferromagnetic transition with a Néel temperature of approximately 20 K. Alternating current (AC) susceptibility at various frequencies suggested a spin-glass-like behavior.

Introduction

Substantial progress has been made over the past two decades in the chemistry of multinary complex transition-metal chalcogenides, which has led to the discovery of several compounds that exhibit interesting physical properties[1,2] and show potential for applications in thermoelectricity,[3–5] spintronics,[6] nonlinear optics,[7] photoelectronics,[8] and solid-state electrolytes.[9–11] Among known complex transition-metal chalcogenides is the fascinating family of ternary MPn_2Q_4 (M = Fe, Mn; Pn = Sb, Bi; and Q = S, Se) compounds with crystal structures that show 1D to 3D connectivity (depending on composition and synthetic method) as well as interesting physical properties.[12–20] For instance, $MnSb_2S_4$ synthesized by solid-state reaction crystallizes in the monoclinic lattice ($mC28$)[18] and is isotypic with $HgBi_2S_4$,[21] whereas an orthorhombic modification ($oP28$),[12,15] isostructural with $FeSb_2S_4$,[13] was obtained from crystals of the same composition isolated from a hydrothermal preparation method. In the crystal structure of the orthorhombic and the monoclinic $MnSb_2S_4$, MnS_6 octahedra share edges to form single chains separated by the Sb_2S_3-type substructure. These isolated chains of MnS_6 octahedra represent the substructure that controls the magnetic properties,[1,2,22,23] whereas the electronic properties of the compound are controlled by the Sb_2S_3-type network that connects adjacent magnetic chains. Because of the unique spatial arrangement of atoms in the MPn_2Q_4 structure, our research group has been very interested in how magnetism and electronic transport respond to modifications of the structure by altering M, Pn, and/or Q. For instance, electrical-conductivity and magnetic-susceptibility measurements revealed that $MnSb_2S_4$ is a semiconducting antiferromagnet with a Néel temperature (T_N) of 26.5 K and an energy bandgap (E_g) of 0.77 eV.[15–17] By modifying the nature of the Sb–S bonds that connect the magnetic and semiconducting subunits in $MnSb_2S_4$ through isoelectronic substitution of S by Se, we anticipate a significant alteration in electronic charge transport as well as the nature of coupling between adjacent magnetic chains. For instance, an energy bandgap smaller than that of $MnSb_2S_4$ (E_g = 0.77 eV) and high electrical conductivity are expected for $MnSb_2Se_4$ due to an increase in the degree of covalency of the Sb–Se bond.

$MnSb_2Se_4$ was first investigated by Kurowski and reported in his doctoral thesis.[15] Based on this work, four

[a] Advanced Materials Research Institute, University of New Orleans,
New Orleans, LA 70148, USA
[b] Department of Chemistry, University of New Orleans,
New Orleans, LA 70148, USA
[c] Department of Chemistry, North Carolina State University,
Raleigh, NC 27695, USA
[d] Department of Physics; University of Michigan,
Ann Arbor, MI 48109, USA
[‡] New address: Materials Science and Engineering Department,
University of Michigan, Ann Arbor, MI 48109, USA
Fax: +1-734-763-4788
E-mail: ppoudeup@umich.edu

different crystal structure models were proposed. The first model obtained from single-crystal structure refinement in the space group *C*2/*m* revealed the Mn(2*a*) site to be randomly occupied by Mn and Sb atoms with nearly equal statistical probability, thus leading to a charge-unbalanced final composition, $Mn_{0.75}Sb_{2.25}Se_4$. The other three models have been obtained from Rietveld refinement using neutron diffraction data. Two of them considered Mn/Sb mixed occupancies at all the Mn and Sb positions and featured very large atomic displacement parameters for both Mn(2*a*) and Mn(2*d*) sites. The last model, which was similar to the ordered structure of $HgBi_2S_4$, also showed large atomic displacement parameters for Mn atoms. Therefore, a conclusive structure model for $MnSb_2Se_4$ could not be obtained from this early study. Another investigation (from the same research) of the $MnSb_{2-x}Bi_xSe_4$ solid solution also revealed large discrepancies in the unit-cell parameters and atomic distribution in $MnSb_2Se_4$.[24] Here, we report an accurate determination of the crystal structure of $MnSb_2Se_4$ by using high-quality single crystals grown from a solid-state reaction of high-purity elements at 500 °C and discuss results of electronic and thermal transport, electronic structure, as well as direct current (DC) and alternating current (AC) magnetic-susceptibility data.

Results and Discussion

Synthesis and Characterization

A single-phase polycrystalline powder of $MnSb_2Se_4$ was obtained through combination of elemental Mn, Sb, and Se at 773 K. Slow heating of the starting mixture to the reaction temperature with intermediate annealing at 573 K was necessary to produce a high-purity phase. Attempts to speed up the reaction by either eliminating the intermediate dwelling step or by slow cooling the starting mixture from the molten state resulted in polycrystalline samples with unreacted selenium as the main impurity phase. Rapid increase of the furnace temperature presumably results in high vapor pressure of the low-melting Se inside the sealed tube, thus leading to a reaction mixture with lower Se content. Upon cooling the furnace to room temperature, the Se vapor ultimately condenses and mixes with the reaction product. X-ray diffraction on polycrystalline powders of the synthesized compound (Figure 1) showed an excellent match with the theoretical pattern simulated from the single-crystal structure refinement. This indicates successful formation of nearly a single phase of $MnSb_2Se_4$ and also attests to the accuracy of the proposed structural model. The accuracy of the structural model, as well as the successful synthesis of $MnSb_2Se_4$, is also supported by the experimental density of 5.65(2) g cm^{-3} (measured using helium-gas pycnometry), which represents approximately 99% of theoretical density calculated from single-crystal structure data (Table 1). $MnSb_2Se_4$ melts congruently at 790 K and shows no sign of decomposition after heating up to 1000 K (Figure 2). Upon cooling, $MnSb_2Se_4$ fully recrystallizes at 771 K, thereby suggesting its high thermal stability. The absence of additional endothermic peaks on heating again suggests the successful synthesis of $MnSb_2Se_4$ as a single phase.

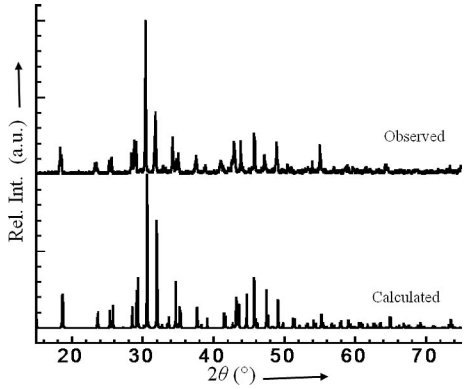

Figure 1. X-ray diffraction pattern of $MnSb_2Se_4$ compared with the theoretical pattern calculated from the single-crystal structure refinement data. The excellent match between both patterns attests to the accuracy of the proposed structural model and also indicates successful synthesis of single-phase polycrystalline powder of $MnSb_2Se_4$.

Table 1. Selected crystallographic data for $MnSb_2Se_4$ at 300 K.

Crystal system; space group	monoclinic; *C*2/*m* (no. 12)
Formula weight [g mol^{-1}]	614.28
Density ($\rho_{calcd.}$) [g cm^{-3}]	5.70
Density ($\rho_{measd.}$) [g cm^{-3}]	5.65(2)
Lattice parameters [Å]	
a [Å]	13.076(3)
b [Å]	3.965(1)
c [Å]	15.236(3)
β [°]	115.1(3)
V [Å^3]	716(2)
Z	4
Crystal size [mm]	0.04 × 0.09 × 0.25
Crystal shape, color	needle, black
Radiation [Å]	λ(Mo-K_α) = 0.71073
μ [cm^{-1}]	295
Diff. elec. density [e Å^{-3}]	+1.36 to –1.35
R_1 [$F_o > 4\sigma(F_o)$][a]	0.027
wR_2 (all)[b]	0.072
GoF	1.124

[a] $R_1 = \Sigma||F_o| - |F_c||/\Sigma|F_o|$. [b] $wR_2 = [\Sigma w(F_o^2 - F_c^2)^2/\Sigma w(F_o^2)^2]^{1/2}$.

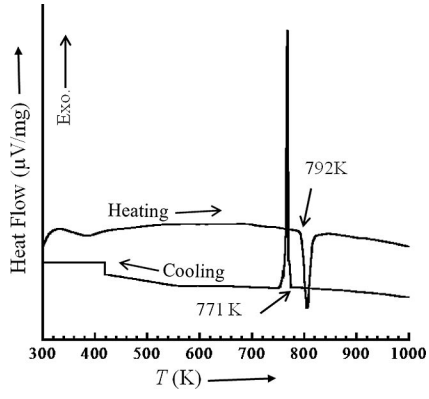

Figure 2. Differential scanning calorimetry (DSC) of $MnSb_2Se_4$ showing a single endothermic peak of congruent melting upon heating as well as a single recrystallization peak upon cooling.

Crystal Structure

$MnSb_2Se_4$ is isostructural with $FeSb_2Se_4$[14] crystallizing in the monoclinic space group $C2/m$ (no. 12) with lattice parameters, a = 13.076(3) Å, b = 3.965(1) Å, c = 15.236(3) Å, β = 115.1(3)° (Table 1). The observed slight increase in the unit-cell parameters of $MnSb_2Se_4$ relative to those of $FeSb_2Se_4$ is consistent with the difference in the effective ionic radii of Mn (0.83 Å) and Fe (0.78 Å) in six-fold coordination.[25] The structure (Figure 3) contains two crystallographically independent Mn atoms located at special positions Mn(3) (2*d*) and Mn(4) (2*a*) (Table 2). The Mn(3) position is fully occupied by Mn, whereas the Mn(4) position contains 19% Sb. Both Mn positions are coordinated by six selenium atoms with Mn(3) located in a distorted [2+4] octahedral geometry with two short axial bonds at 2.550(2) Å and four long equatorial bonds at 2.721(2) Å, whereas Mn(4) is found in an almost regular octahedral geometry with bond lengths that range between 2.676(2) Å and 2.702(2) Å. Along [010], adjacent $\{Mn(3)\}Se_{2+4}$ octahedra share edges to form one-dimensional (1D) $[\{Mn(3)\}Se_{2+4}]_\infty$ chains (Figure 3, b), which are weakly linked [through an Sb(1)–Se(2) bond of 3.116(2) Å] along the *a* axis by the Sb(1) atom in a distorted [1+2+2] square pyramid of Se atoms (Table 3) to build a slab denoted *B* parallel to the *ab* plane. A similar type of slab denoted *A* is formed by interconnecting [through the Sb(2)–Se(4) bond of 3.093(2) Å] 1D $[\{Mn(4)\}Se_6]_\infty$ chains (Figure 3, c) parallel to [010] with Sb(2) atoms in a distorted [1+2+2+1] octahedral coordination (Figure 3, A). Both *A* and *B* slabs are linked along the *c* axis by a rather long Sb(2)–Se(3) bond [3.138(2) Å] to build the three-dimensional (3D) structure. Alternatively, the structure of $MnSb_2Se_4$ can be better described as a one-dimensional arrangement of $[\{Mn\}\{Sb\}_2\{Se\}_4]_\infty$ chains of edge-sharing octahedra parallel to [010], thus giving the rather long Sb–Se bonds (dashed bonds in Figure 3, a) interconnecting individual chains.

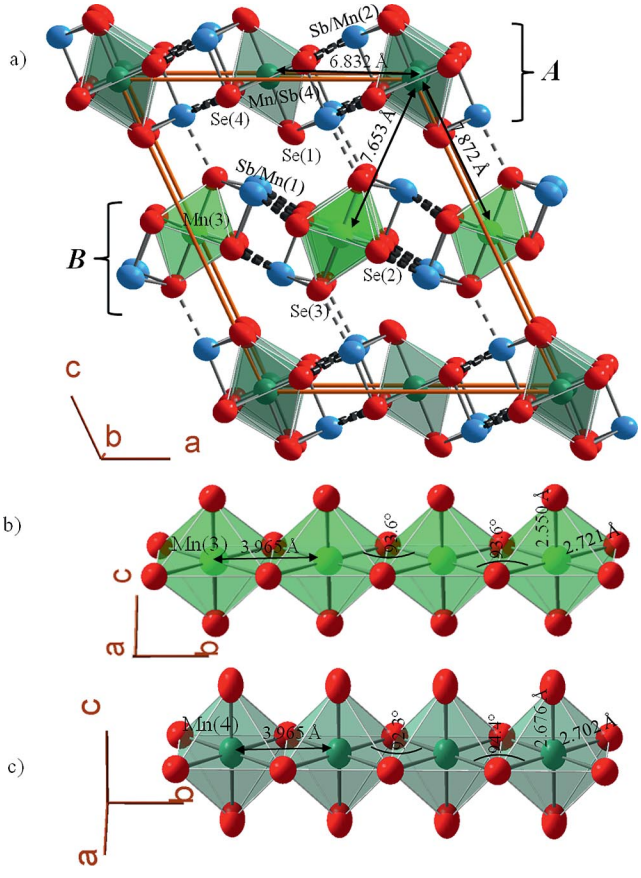

Figure 3. (a) Graphic representation of the crystal structure of $MnSb_2Se_4$ projected along the *b* axis highlighting the separation between 1D chains of edge-sharing $\{Mn\}Se_6$ octahedra. Ellipsoids are set at 98% probability level for all atoms, and a bond threshold of 3.14 Å was used. Dashed bonds are weak Sb–Se connecting adjacent 1D $[\{Mn\}\{Sb\}_{4/2}\{Se\}_{2+4/2}]_\infty$ structural subunits. Geometrical details of 1D chains of edge-sharing Mn-centered (b) $\{Mn(3)\}Se_{2+4}$ and (c) $\{Mn(4)\}Se_6$ octahedra running along [010].

Table 2. Atomic coordinates, Wyckoff positions (W.P.), site-occupancy factors (k), and equivalent isotropic displacement parameters $U_{eq}/10^{-4}$ Å^2 for all atoms in the asymmetric unit of $MnSb_2Se_4$.

Atom	W.P.	k	x	y	z	U_{eq}[a]
Sb(1)	4*i*	0.95	0.2738(2)	0	0.6334(2)	267(3)
Mn(1)	4*i*	0.05	0.2738(2)	0	0.6334(2)	267(3)
Sb(2)	4*i*	0.96	0.3554(2)	0	0.1260(2)	242(3)
Mn(2)	4*i*	0.04	0.3554(2)	0	0.1260(2)	242(3)
Mn(3)	2*d*		0	1/2	1/2	265(7)
Sb(4)	2*a*	0.19	0	0	0	252(9)
Mn(4)	2*a*	0.81	0	0	0	252(9)
Se(1)	4*i*		0.0123(2)	0	0.1799(2)	269(4)
Se(2)	4*i*		0.1143(2)	0	0.4575(2)	228(4)
Se(3)	4*i*		0.3446(2)	0	0.3277(2)	243(4)
Se(4)	4*i*		0.6549(2)	0	0.0533(2)	246(4)

[a] U_{eq} is defined as one-third of the trace of the orthogonalized U_{ij} tensor.

Table 3. Selected interatomic distances [Å] in $MnSb_2Se_4$ at 300 K.[a]

Sb(1)|Mn(1)–Se(2)	2.607(2)	Mn(3)–Se(3)^{ii}	2.550(2)
Sb(1)|Mn(1)–Se(3)^{i}	2.731(2)	Mn(3)–Se(3)^{vii}	2.550(2)
Sb(1)|Mn(1)–Se(3)^{ii}	2.731(2)	Mn(3)–Se(2)^{viii}	2.721(2)
Sb(1)|Mn(1)–Se(2)^{ii}	3.116(2)	Mn(3)–Se(2)^{ix}	2.721(2)
Sb(1)|Mn(1)–Se(2)^{i}	3.116(2)	Mn(3)–Se(2)	2.721(2)
Sb(1)|Mn(1)–Se(1)^{ii}	3.620(2)	Mn(3)–Se(2)^{x}	2.721(2)
Sb(1)|Mn(1)–Se(1)^{i}	3.620(2)		
		Mn(4)|Sb(4)–Se(1)	2.676(2)
Sb(2)|Mn(2)–Se(4)^{iii}	2.674(2)	Mn(4)|Sb(4)–Se(1)^{xi}	2.676(2)
Sb(2)|Mn(2)–Se(1)^{iv}	2.718(2)	Mn(4)|Sb(4)–Se(4)^{xii}	2.702(2)
Sb(2)|Mn(2)–Se(1)^{v}	2.718(2)	Mn(4)|Sb(4)–Se(4)^{vii}	2.702(2)
Sb(2)|Mn(2)–Se(4)^{vi}	3.093(2)	Mn(4)|Sb(4)–Se(4)^{xiii}	2.702(2)
Sb(2)|Mn(2)–Se(4)^{vii}	3.093(2)	Mn(4)|Sb(4)–Se(4)^{vi}	2.702(2)
Sb(2)|Mn(2)–Se(3)	3.138(2)		

[a] Operators for generating equivalent atoms: (i) 1/2 – x, –1/2 – y, 1 – z; (ii) 1/2 – x, 1/2 – y, 1 – z; (iii) 1 – x, –y, –z; (iv) 1/2 + x, 1/2 + y, z; (v) 1/2 + x, –1/2 + y, z; (vi) –1/2 + x, –1/2 + y, z; (vii) –1/2 + x, 1/2 + y, z; (viii) x, 1 + y, z; (ix) –x, –y, 1 – z; (x) –x, 1 – y, 1 – z; (xi) –x, –y, –z; (xii) 1/2 – x, –1/2 – y, –z; (xiii) 1/2 – x, 1/2 – y, –z.

Magnetism

Figure 4 (a) shows the magnetic susceptibility and the inverse susceptibility of the synthesized polycrystalline powders of $MnSb_2Se_4$ measured at 100 and 1000 Oe. The susceptibility exhibits a broad peak at 20 K, which suggests an ordering of Mn magnetic moments at low temperatures. The susceptibility data above 120 K could be fitted to the Curie–Weiss law with a Curie constant of 5.48 emu K mol^{-1} and a Weiss constant of –74 K. The corresponding effective magnetic moment is μ_{eff} = 5.82(2) μ_B per Mn atom. This value is relatively close to the expected theoretical value of $\mu_{eff} \approx 5.92\ \mu_B$ for Mn^{2+} ($3d^5$) in the high-spin configuration, thereby confirming our assignment of the oxidation state of Mn ions (2+) in the crystal structure. The large negative value of the Weiss constant indicates that the interaction between the Mn^{2+} magnetic moments is predominantly antiferromagnetic (AFM). However, the slight increase in the susceptibility observed below 5 K (Figure 4, a, inset) also suggests the existence of a small ferromagnetic (FM) ordering in the sample at very low temperatures. In addition, the observed strong dependence of the magnetic susceptibility below 20 K on the applied magnetic field, the shift of the blocking temperature to lower values with the increase in the applied magnetic field, as well as the difference between the ZFC and FC data suggests competing magnetic ordering similar to spin-glass behavior within the sample.[26] To better assess this magnetic behavior, AC susceptibility measurements at various frequencies and different amplitudes of the excitation field were performed. Figure 4 (b) shows the in-phase part, χ', of the AC susceptibility of $MnSb_2Se_4$ for selected frequencies between 500 and 10000 Hz. The amplitudes and positions of the peak maxima (T_{max}) depend on the frequency of the applied AC magnetic field (Figure 4, b, inset). T_{max} gradually shifts to higher temperatures, and the peak intensity decreases with increasing frequency, which indicates that the peaks are associated with the onset of spin freezing. These features are typical for classical spin-glass systems such as $Cu_{1-x}Mn_x$ and $Au_{1-x}Mn_x$ alloys.[26–29] A quantitative measure of the change in the freezing temperature with frequency in spin-glass materials is obtained by calculating the Mydosh parameter (K) defined as the relative shift of the maximum temperature (T_{max}) per decade of frequency.[26] The estimated $K = \Delta T_m/[T_m \log(\omega)] = 0.013$ is about three times higher than K values found in spin-glass systems such as $Cu_{1-x}Mn_x$ (K = 0.005) and $Au_{1-x}Mn_x$ (K = 0.0045) and suggests that the relaxation behavior is consistent with a spin-glass-like behavior. However, in most spin-glass systems, the magnitude of the AC susceptibility below T_{max} is frequency-dependent and becomes independent of the frequency above T_{max}.[30] Therefore, the observed dependence of the magnitude of the AC susceptibility above and below T_{max} upon frequencies (Figure 4, b, inset) suggests that the downturn on the magnetic-susceptibility curves (ZFC and FC) of $MnSb_2Se_4$ is more complicated in nature. A tentative explanation of this behavior is provided below.

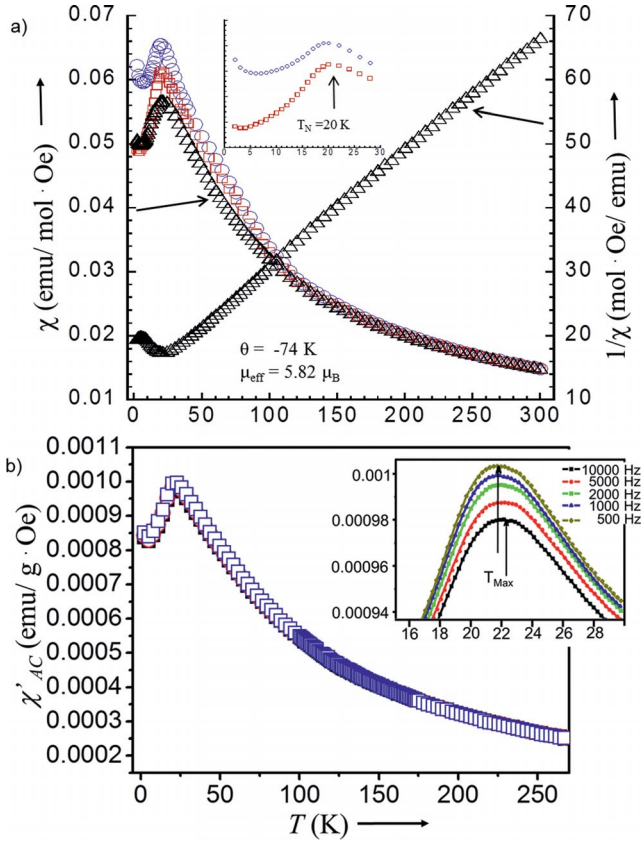

Figure 4. (a) Temperature dependence of the field-cooled (FC) and zero-field-cooled (ZFC) molar magnetic susceptibility and inverse susceptibility of $MnSb_2Se_4$ measured under applied field of 100 and 1000 Oe. Blue circle: FC at 100 Oe; red square: ZFC at 100 Oe; black triangle: ZFC at 1000 Oe. The inset is the magnification of the susceptibility around $T_N \approx 20$ K. (b) Temperature dependence of the in-phase component of the AC susceptibility measured for various applied frequencies from 500 Hz to 10 kHz under an applied field of 10 Oe. The inset is a magnification of the portion of the curves around the maximum χ'. Black symbols: 10 kHz; red symbols: 5 kHz; green symbols: 2 kHz; blue symbols: 1000 Hz; yellow symbols: 500 Hz.

To understand the magnetic behavior of $MnSb_2Se_4$, we have carefully analyzed geometrical details of the $[MnSe_6]_\infty$ magnetic chains, their arrangement in the 3D structure, and the coupling (intrachain and interchain) between localized spins on adjacent Mn atoms by using the Goodenough–Kanamori rules.[31–33] As described above, the Mn3 atom is located in a distorted octahedral geometry, [{Mn(3)}Se_{2+4}] with two apical short bonds [2.550(2) Å] and four equatorial long bonds [2.721(2) Å]. Despite the fact that Mn^{2+} ($3d^5$) is not a Jahn–Teller ion, this kind of severe distortion of the octahedral coordination results in a Jahn–Teller-type splitting of the d orbitals, thus leading to an increase in the energy level of d_{z^2}, d_{xz} and d_{yz} orbitals. This suggests the orbital and spin distribution $(d_{xy})^1(d_{xz}, d_{yz})^1(d_{x^2-y^2})^1(d_{z^2})^1$ leads to a total spin value of S = 5/2 (high spin). The more regular octahedral coordination of the Mn(4) atom [{Mn(4)}Se_6] suggests an octahedral splitting of $3d^5$ orbitals with spin distribution of $(d_{xz}, d_{yz}, d_{xy})^1(d_{z^2}, d_{x^2-y^2})^1$, which corresponds to a total spin value of S = 5/2 (high spin). The total number of spin, S = 5/2 for both Mn3 and

Mn4 atoms, is consistent with the effective magnetic moment calculated from the magnetic-susceptibility data. The structure of $MnSb_2Se_4$ can therefore be regarded as layers A and B of magnetic chains alternating along the *c* axis. The magnetic behavior of $MnSb_2Se_4$ therefore depends on the interactions between adjacent magnetic atoms within a single chain (intrachain) and/or the interchain interactions. The shortest distance between magnetic chains in adjacent magnetic layers is around 7.653 Å, and the intralayer separation between magnetic chains is around 6.832 Å (Figure 3, a). These distances are too long for direct or indirect magnetic exchange interactions between neighboring magnetic chains, thereby suggesting that $MnSb_2Se_4$ is a quasi-1D magnetic system. Therefore, the magnetic behavior of the compound is controlled by the nature and magnitude of exchange interactions between adjacent magnetic atoms in $[\{Mn(3)\}Se_6]_\infty$ and $[\{Mn(4)\}Se_6]_\infty$ magnetic chains. However, Mn atoms within individual chains (along [010]) are 3.965 Å apart (Figure 3, b). This separation is too long for direct magnetic exchange interactions between the magnetic moments on neighboring Mn atoms. Therefore, adjacent Mn(3) and Mn(4) atoms are magnetically coupled by indirect exchange interactions through the bridging Se atoms. For instance, the observed Mn(3)–Se(2)–Mn(3) bond angle of 93.6° within the $[\{Mn(3)\}Se_6]_\infty$ chain suggests antiferromagnetic or weak ferromagnetic coupling of spins localized on adjacent Mn(3) atoms. Within the $[\{Mn(4)\}Se_6]_\infty$ chain, two Mn(4)–Se(4)–Mn(4) coupling paths with bond angles of 92.3 and 94.4° are possible, thereby indicating competition between AFM and FM ordering of spins localized on adjacent Mn(4) atoms (Figure 3, c). This magnetic frustration within the $[\{Mn(3)\}Se_6]_\infty$ and $[\{Mn(4)\}Se_6]_\infty$ chains are believed to be responsible for the observed broad downturn of the magnetic susceptibility at 20 K as well as the frequency dependence of the peak ($T_{max,}$) position and amplitude. Upon cooling the sample below 5 K, the FM coupling presumably begins to dominate, thus leading to the observed increase in the DC magnetic susceptibility.

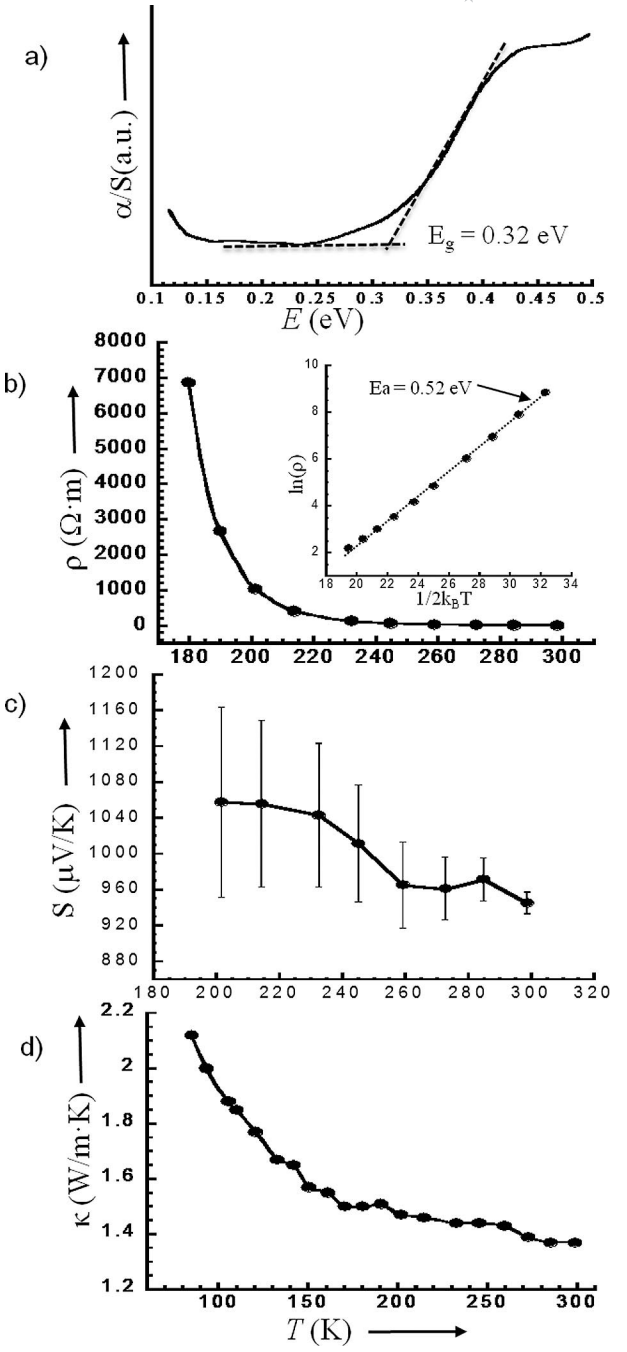

Figure 5. (a) Room-temperature diffuse reflectance infrared spectrum of $MnSb_2Se_4$ showing a narrow optical bandgap. Temperature dependence of electronic and thermal charge transport of $MnSb_2Se_4$: (b) electrical resistivity; (c) Seebeck coefficient; (d) thermal conductivity. The sharp increase in the electrical resistivity around 230 K is attributed to a semiconductor-to-insulator (SI) transition. The inset of (b) shows the plot of $\ln(\rho)$ versus $1/2k_BT$ from which the bandgap of 0.52 eV was estimated.

Optical and Charge-Transport Properties

The diffuse reflectance infrared absorption spectrum of $MnSb_2Se_4$ was recorded at room temperature in the range 0.05–0.5 eV. The bandgap estimated from the absorption coefficient/scattering coefficient (α/S) ratio versus energy plot is about 0.32 eV, which indicates that the compound is a narrow-bandgap semiconductor at 300 K (Figure 5, a). The observed value of the energy gap is comparable to the optical bandgap of $FeSb_2Se_4$ (E_g = 0.33 eV)[14] and is consistent with the black color of the $MnSb_2Se_4$ crystals. The temperature dependence of the electrical resistivity (ρ) of $MnSb_2Se_4$ was measured from 100 to 300 K (Figure 5, b). At room temperature, the electrical resistivity is approximately 8.9 Ωm and slightly increases with decreasing temperature down to about 230 K. This trend is consistent with the semiconducting nature of the compound. The observed large value of the electrical resistivity of $MnSb_2Se_4$ at 300 K presumably originates from the quasi-1D nature of the crystal structure in which individual $[\{Mn\}Se_6]_\infty$ chains parallel to [010] are only weakly interconnected along [100] and [001] through long Sb–Se bonds to the 3D network (Figure 3, a). The resistivity rises rapidly with further decreases in the temperature, and below 180 K, it attained such high

values (>10 kΩm) that the noise precluded collection of the data (Figure 5, b). The rapid increase in the resistivity is similar to the one observed in $FeSb_2Se_4$.[14] From the Arrhenius plot (Figure 5, b, inset), we calculate the bandgap value to be 0.52 eV. This value is consistent with the observed optical bandgap, thereby confirming again the semiconducting character of $MnSb_2Se_4$ at 300 K. Figure 5 (c) shows the temperature dependence of the Seebeck coefficient of $MnSb_2Se_4$ from 200 to 300 K. Positive values of the Seebeck coefficient were observed in the whole measured temperature range, thereby indicating that $MnSb_2Se_4$ is a *p*-type narrow-gap semiconductor. The Seebeck data have progressively larger error bars as the temperature decreases due to the noise on the Seebeck voltage contacts associated with the rapid rise in electrical resistivity. The Seebeck coefficient at 300 K is around 950 $\mu V K^{-1}$ and gradually increases with the decreasing temperature to a value of about 1050 $\mu V K^{-1}$ at 200 K. The temperature dependence of the total thermal conductivity of $MnSb_2Se_4$ is shown in Figure 5 (d). Because of the large electrical resistivity of $MnSb_2Se_4$ in the measured temperature range, the electronic contribution to the thermal conductivity ($\kappa_{elc.}$) is negligible. Therefore, the observed thermal conductivity values essentially correspond to the lattice contribution ($\kappa_{lat.}$). At 300 K, the lattice thermal conductivity of $MnSb_2Se_4$ is 1.4 $W m^{-1} K^{-1}$ (Figure 5, d). This low value of the lattice thermal conductivity of $MnSb_2Se_4$ can be attributed to the combination of low crystal symmetry and complex structure and chemical composition with heavy elements such as Sb and Se. The lattice thermal conductivity of $MnSb_2Se_4$ gradually increases with decreasing temperature and a $\kappa_{lat.}$ value of 2.1 $W m^{-1} K^{-1}$ was measured at 90 K. The observed increase in the lattice thermal conductivity with decreasing temperature is consistent with a gradual freezing of phonon umklapp processes.

Electronic Structure

Electronic band structure calculations of $MnSb_2Se_4$ show a small energy gap of around 0.3 eV in a narrow window around the Fermi level (E_F) (Figure 6, a). This value is consistent with the observed optical bandgap as well as the activation energy near room temperature, thus further confirming the room-temperature semiconducting character of $MnSb_2Se_4$. The site-projected density of states (DOS) for one formula unit of nonmagnetic $MnSb_2Se_4$ (Figure 6, b), shows that the highest-occupied states cross the Fermi level at high density of states, which is attributed to Mn^{2+} t_{2g} states. The next occupied bands above E_F are formed by Mn^{2+} e_g states. The electron distribution of the d orbital could be $t_{2g}^3(d_{xy}, d_{xz}, d_{yz})^1$ and $e_g^2(d_{x^2-y^2}, d_{z^2})^1$, thus confirming the magnetic effective moment calculated from magnetic-susceptibility data. The large broad bands in the energy range from –4 to –1 eV are dominated by bonding p states of Sb and Se, whereas the bottom of the conduction band is based mainly on empty Mn p orbitals. The analysis of bonding interactions between atoms in $MnSb_2Se_4$ by using the crystal orbital Hamiltonian population (COHP) method[34] showed that the major part of the valence band between –3 and –1 eV is dominated by Mn–Se bonding interactions, whereas at the top of the valence band, Sb–Se and Mn–Se interactions dominate the antibonding interactions (Figure 6, c). The Mn(3)–Se interactions contribute more strongly to the covalent bonding than Mn(4)–Se in the energy range of –3 to –1 eV, and around the Fermi level both Mn(3)–Se and Mn(4)–Se equally contribute to the antibonding. Despite the significant antibonding interactions at E_F, the compound is stable because of the positive values of integrants, –ICOHP (Table 4), which predominantly emphasize the bonding character of orbitals below E_F. Above the Fermi level, all states are strongly antibond-

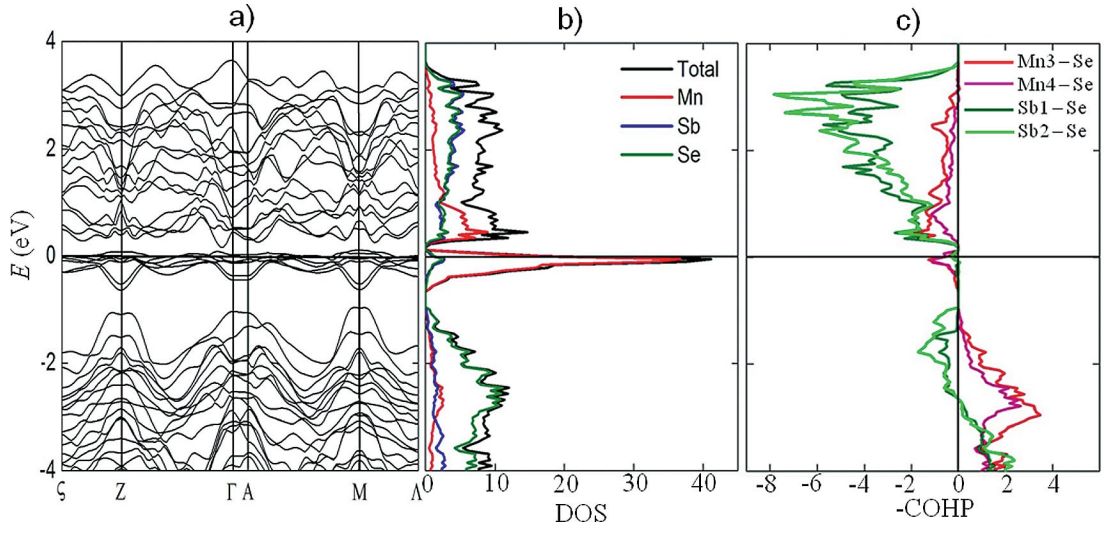

Figure 6. (a) Electronic band structure of $MnSb_2Se_4$ near the Fermi energy showing a small energy gap of around 0.3 eV. (b) Site-projected total density of states (DOS) and partial density of states for Mn, Sb, and Se atoms. (c) Crystal orbital Hamiltonian populations (COHP) for selected Mn(3)–Se, Mn(4)–Se, Sb(1)–Se, and Sb(2)–Se interactions.

ing, which suggests destabilization of the compound upon atomic substitutions by more electron-rich elements if the crystal structure of the phase remained the same.

Table 4. –ICOHP for the Sb(1), Sb(2), Mn(3), and Mn(4) sites in $MnSb_2Se_4$.

Bond	No.	Bond length	–ICOHP
Mn3–Se2	4	2.721(2)	1.26
Mn3–Se3	2	2.550(2)	1.86
Mn4–Se1	2	2.676(2)	1.81
Mn4–Se4	4	2.702(2)	1.53
Sb1–Se2	2	3.116(2)	0.21
Sb1–Se2	1	2.607(2)	2.32
Sb1–Se3	2	2.731(2)	1.64
Sb2–Se1	2	2.718(2)	1.77
Sb2–Se3	1	3.138(2)	0.22
Sb2–Se4	1	2.674(2)	1.88
Sb2–Se4	2	3.093(2)	0.32
Sb1–Se1	2	3.622(2)	0.01

Conclusion

A single phase of the monoclinic $MnSb_2Se_4$ phase was successfully synthesized by solid-state reaction of the elements at 773 K and an accurate structural model was proposed by using single-crystal diffraction data. The compound crystallizes isostructurally with $FeSb_2Se_4$[14] and exhibits Mn/Sb mixed occupancy at the Mn-rich M(4)(2*a*) site, as well as in all Sb-rich M(1) and M(2) positions. Charge-transport data, diffuse reflectance infrared spectroscopy, and electronic structure calculations revealed that $MnSb_2Se_4$ is a narrow-gap *p*-type semiconductor with E_g = 0.32 eV and exhibits a sharp increase in the resistivity below 180 K. The compound displays a low lattice thermal conductivity (ca. 1.4 $W m^{-1} K^{-1}$ at 300 K), melts congruently at 790 K, and is thermally stable up to 1000 K. DC and AC magnetic-susceptibility measurements and the analysis of the geometrical parameters within the $[\{Mn\}Se_6]_\infty$ single chains in light of the Goodenough–Kanamori rules[31–33] strongly suggest that $MnSb_2Se_4$ is not an ordinary antiferromagnet in which all the magnetic spins are antiparallel below T_N = 20 K. The magnetism within individual chains in $MnSb_2Se_4$ is rather controlled by competing interactions.

Experimental Section

Synthesis: A single phase of $MnSb_2Se_4$ was synthesized by solid-state reaction of the elements in the stoichiometric ratio. All reagents (99.999% purity) were used as purchased from the supplier (Cerac). The starting materials in their powder form, weighed in the desired ratio under argon atmosphere in a dry glovebox (total mass: 10 g), were roughly mixed using a mortar and pestle and sealed in an evacuated quartz tube (ca. 10^{-3} Torr). The sealed tube was loaded into a tube furnace and heated slowly to 573 K over 12 h. This heating rate was required to prevent explosive reactions of the low-melting Se with Mn and/or Sb. The temperature was held at 573 K for 48 h to allow complete melting of Se and reaction with the remaining Mn and Sb powders. The temperature was then ramped up to 773 K over 12 h and remained there for 72 h until finally being cooled slowly to room temperature over 48 h. Several needle-shaped black crystals suitable for single-crystal X-ray structure determination were selected from the resulting polycrystalline product. The remaining sample was ground to a powder, and a high density (>95%) pellet for physical properties measurements was fabricated using a uniaxial hot press.

Powder X-ray Diffraction (PXRD): To assess the phase purity of the synthesized polycrystalline powder, PXRD data were collected using curved graphite crystal monochromated Cu-K_α radiation (λ = 1.54056 Å) in reflection geometry with a Philips X-ray powder diffractometer equipped with a position sensitive scintillation counter and operating at 45 kV and 40 mA. The experimental X-ray diffraction pattern was subsequently matched with the theoretical pattern simulated by using single-crystal structure data.

Single-Crystal Structure Refinement: A black needle-shaped single crystal of $MnSb_2Se_4$ with approximate dimensions of $0.04 \times 0.09 \times 0.25$ mm^3 was used for X-ray data collection. Intensity data were recorded at 300 K with a STOE Imaging Plate Diffraction System (IPDS-2T) using graphite-monochromated Mo-K_α radiation (λ = 0.71073 Å) and were indexed in the monoclinic crystal system with cell parameters a = 13.076(6) Å, b = 3.9651(8) Å, c = 15.236(4) Å and β = 115.1(1)°, which are similar to the unit-cell parameters of $FeSb_2Se_4$.[14] Therefore, atomic positions of $FeSb_2Se_4$ were used as starting model for the structure refinement in the space group *C*2/*m* (no. 12) using the SHELTXL package.[35] Initially, Sb atoms were assigned to the general positions M(1)(4*i*) and M(2)(4*i*) located respectively in a distorted octahedral and square-pyramidal coordination, whereas Mn atoms were located in special positions M(3)(2*d*) and M(4)(2*a*) with octahedral coordination. The refinement of this model using full-matrix least-squares techniques resulted in R_1 = 5% with reasonable thermal parameters for all atoms except Mn(4), which displayed a smaller thermal parameter than those of the Sb atoms. This suggested Mn/Sb mixed occupancy at the M(4) position. To allow for a charge-balanced final composition, Sb/Mn mixed occupancy at the M(1), M(2), and M(3) positions was also considered. The refinement of this model resulted in more uniform thermal parameters for all atoms and an almost neutral composition with about 5% Mn in each of the Sb(1) and Sb(2) sites, whereas the M(3) position remained fully occupied by Mn. In the final refinement cycles, an electro-neutrality restraint was included along with a secondary extinction correction and anisotropic displacement parameters for all atoms. The occupancy factors at M(1), M(2), and M(4) positions were refined to the final values of M(1) = 95%, Sb + 5% Mn, M(2) = 96% Sb + 4% Mn, and Mn(4) = 81% Mn + 19% Sb, which led to the final charge-balanced composition $Mn_{0.995(3)}Sb_{2.005(3)}Se_4$ assuming 2+, 3+, and 2– oxidation states for Mn, Sb, and Se, respectively. The final assignment of Sb and Mn atoms at metal positions and the suggested oxidation state for Sb and Mn atoms in $MnSb_2Se_4$ are consistent with the results of bond valence sum (BVS) calculations[36] [Sb(1): 2.8; Sb(2): 2.8; Mn(3): 2.3; Mn(4): 2.2]. Summary of crystallographic data for $MnSb_2Se_4$ are given in Table 1. The atomic coordinates and isotropic displacement parameters of all atoms are given in Table 2. Selected interatomic distances are gathered in Table 3. The software Diamond[37] was utilized to create the graphic representation of the crystal structure with an ellipsoid representation (98% probability level) for all atoms.

Further details of the crystal structure investigation can be obtained from the Fachinformationszentrum Karlsruhe, 76344 Eggenstein-Leopoldshafen, Germany (fax: +49-7247-808-666; E-mail: crysdata@fiz.karlsruhe.de) on quoting the depository number CSD-421940.

Differential Scanning Calorimetry (DSC): Differential scanning calorimetry data were recorded with a 404-F1 DSC apparatus (NETZSCH) by using approximately 15 mg of the synthesized compound sealed in a small quartz tube under a residual pressure of ca. 10^{-3} Torr. An equivalent mass of alumina (Al_2O_3) was used as the reference. The sample and reference were simultaneously heated to 1073 K at a rate of 20 K min^{-1}, isothermed for 2 min, and then cooled to 423 K at a rate of 20 K min^{-1}. DSC data were recorded during two heating and cooling cycles. The endothermic onset temperature is reported as the melting point, and the exothermic onset temperature is the crystallization point.

Infrared Spectroscopy: To probe the optical bandgap of $MnSb_2Se_4$, room-temperature diffuse reflectance infrared spectroscopy was performed in the 4000–400 cm^{-1} region with a Thermo Nicolet NEXUS 670 FTIR spectrometer. The reflectance data were converted into absorption data by using the Kulbelka–Munk function $\alpha/S = (1 - R)^2/2R$[38] (in which R is the reflectance at a given wavelength, α is the absorption coefficient, and S is the scattering coefficient), and the optical bandgap was estimated from an absorption (α/S)[38,39] versus energy plot.

Magnetic Measurements: DC and AC magnetic-susceptibility measurements were performed on polycrystalline $MnSb_2Se_4$ powder (53 mg) with a superconducting quantum interference device (SQUID). DC susceptibility data in FC and ZFC modes were recorded over a temperature range from 2 K to 300 K with an applied field of 100 and 1000 Oe. AC susceptibility data at various frequencies (500 Hz to 10 kHz) were recorded between 2 and 300 K in an applied field of 10 Oe.

Charge-Transport Measurements: A rectangular-shaped specimen with dimensions of $2.4 \times 2.6 \times 11$ mm^3 cut from a 96% dense hot-pressed pellet of $MnSb_2Se_4$ was used for low-temperature measurements of electrical conductivity, the Seebeck coefficient, and thermal conductivity. Electrical conductivity was measured by a four-probe method by using a high-sensitivity AC bridge with an excitation frequency of 17 Hz. The Seebeck coefficient and the thermal conductivity at $T \leq 300$ K were measured by using a longitudinal steady-state technique with calibrated Au:Fe/Chromel-P thermocouples (Omega Corp.) traceable to the National Institute of Standards and Technology (NIST) standards and with copper leads serving as voltage probes.

Electronic Structure Calculations: The electronic structure of $MnSb_2Se_4$ was calculated with the linear muffin-tin orbital (LMTO) method in the atomic sphere approximation (ASA) by using the tight-binding program TB-LMTO-ASA.[40] A charge-balanced model was constructed by assigning Sb atoms at M(1) and M(2) positions, whereas Mn atoms were located at the M(3) and M(4) sites. The radii of the Wigner–Seitz (WS) spheres were assigned automatically so that the overlapping potentials would be the best possible approximations to the full potentials, and an interstitial sphere was necessary with the default 16% overlap restriction.[40] Since the structure of $MnSb_2Se_4$ is rather open, special care was taken in filling the interatomic space. Using only atom-centered spheres resulted in errors because of overlaps that were too large. Therefore, the empty interstitial spheres (ES) were added to the crystal potential and the basis set. The sphere radii and their positions were chosen so that space-filling was achieved without exceeding a sphere overlap of 16%. All sphere positions and radii were calculated automatically; the WS radii [Å] were Mn 1.47–1.57, Sb 1.57–1.61, Se 1.45–1.53, and ES 0.74–1.33. The calculations used a basis set of Mn-4s/4p/3d, Sb-5s/5p, and Se-4s/4p orbitals and the reciprocal space integrations were performed on $12 \times 12 \times 12$ grids of irreducible k points by using the tetrahedron method.[41,42]

Acknowledgments

This work was supported by the National Science Foundation (CAREER Award DMR-0954817), the Louisiana Board of Regents [grant number NSF(2008)-PFUND-126], and the University of New Orleans Office of Research and Sponsored Programs (SCoRe2009 award). The authors thank Prof. John Wiley (UNO) for granting access to his group's X-ray powder diffractometer. Transport measurements at the University of Michigan are supported as part of the Revolutionary Materials for Solid-State Energy Conversion, an Energy Frontier Research Center funded by the US Department of Energy, Office of Science, Office of Basic Energy Science under award number DE-SC001054.

[1] Y. Matsushita, Y. Ueda, *Inorg. Chem.* **2003**, *42*, 7830.
[2] Y. Matsushita, Y. Ueda, *Inorg. Chem.* **2006**, *45*, 2022.
[3] D. Y. Chung, T. Hogan, P. Brazis, M. Rocci-Lane, C. Kannewurf, M. Bastea, C. Uher, M. G. Kanatzidis, *Science* **2000**, *287*, 1024.
[4] M. G. Kanatzidis, *Semicond. Semimetals* **2001**, *69*, 51.
[5] D. M. Rowe, in: *Handbook of Thermoelectrics*, CRC Press, Boca Raton, FL, **1995**.
[6] S. A. Wolf, D. D. Awschalom, R. A. Buhrman, J. M. Daughton, S. Von Molnar, M. L. Roukes, A. Y. Chtchelkanova, D. M. Treger, *Science* **2001**, *294*, 1488.
[7] A. A. Ballman, R. L. Byer, D. Eimerl, R. S. Feigelson, B. J. Feldman, L. S. Goldberg, N. Menyuk, C. L. Tang, *Appl. Opt.* **1987**, *26*, 224.
[8] S. Ibuki, S. Yoshimatsu, *J. Phys. Soc. Jpn.* **1955**, *10*, 549.
[9] R. Kanno, T. Hata, Y. Kawamoto, M. Irie, *Solid State Ionics* **2000**, *130*, 97.
[10] Y. Matsushita, M. G. Kanatzidis, *Z. Naturforsch. B* **1998**, *53*, 23.
[11] S. Shionoya, W. M. Yen, in: *Phosphor Handbook*, CRC Press, Boca Raton, FL, **1999**.
[12] K. Bente, A. Edenharter, *Z. Kristallogr.* **1989**, *186*, 31.
[13] M. J. Buerger, T. Hahn, *American Mineralogist* **1955**, *40*, 226.
[14] H. Djieutedjeu, P. F. P. Poudeu, N. J. Takas, J. P. A. Makongo, A. Rotaru, K. G. S. Ranmohotti, C. J. Anglin, L. Spinu, J. B. Wiley, *Angew. Chem. Int. Ed.* **2010**, *49*, 9977.
[15] D. Kurowski, *PhD Thesis*, University of Regensburg, Germany, **2003**.
[16] P. Leone, C. Doussier-Brochard, G. Andre, Y. Moelo, *Phys. Chem. Miner.* **2008**, *35*, 201.
[17] S. F. Matar, R. Weihrich, D. Kurowski, A. Pfitzner, V. Eyert, *Phys. Rev. B* **2005**, *71*, 2350271.
[18] A. Pfitzner, D. Kurowski, *Z. Kristallogr.* **2000**, *215*, 373.
[19] C. Tian, C. Lee, E. Kan, F. Wu, M.-H. Whangbo, *Inorg. Chem.* **2010**, *49*, 10956.
[20] M. Wintenberger, G. Andre, *Phys. B* **1989**, *156*, 315.
[21] W. G. Mumme, J. A. Watts, *Acta Crystallogr., Sect. B* **1980**, *36*, 1300.
[22] P. Leone, G. Andre, C. Doussier, Y. Moelo, *J. Magn. Magn. Mater.* **2004**, *284*, 92.
[23] P. Leone, L. M. Le Leuch, P. Palvadeau, P. Molinie, Y. Moelo, *Solid State Sci.* **2003**, *5*, 771.
[24] A. Lecker, D. Kurowski, A. Pfitzner, *Z. Anorg. Allg. Chem.* **2006**, *632*, 2144.
[25] R. D. Shannon, *Acta Crystallogr., Sect. A* **1976**, *32*, 751.
[26] J. A. Mydosh, *Spin Glasses: An Experimental Introduction*, Taylor & Francis, London, Washington, DC, **1993**.
[27] K. Binder, A. P. Young, *Rev. Mod. Phys.* **1986**, *58*, 801.
[28] K. H. Fisher, J. A. Hertz, *Spin Glasses*, Cambridge University Press, Cambridge, **1991**.

[29] M. J. P. Gingras, C. V. Stager, B. D. Gaulin, N. P. Raju, J. E. Greedan, *J. Appl. Phys.* **1996**, *79*, 6170.
[30] P. Wang, Z. M. Stadnik, J. Żukrowski, B. K. Cho, J. Y. Kim, *Phys. Rev. B* **2010**, *82*, 134404.
[31] J. B. Goodenough, *Phys. Rev.* **1955**, *100*, 564.
[32] J. B. Goodenough, *J. Phys. Chem. Solids* **1958**, *6*, 287 .
[33] J. Kanamori, *J. Phys. Chem. Solids* **1959**, *10*, 87.
[34] R. Dronskovski, P. E. Bloechl, *J. Phys. Chem.* **1993**, *97*, 8617.
[35] G. M. Sheldrick, *SHELTXL*, v6.12, Bruker Analytical X-ray Instruments, Inc., Madison, WI, **2000**.
[36] N. E. Brese, M. Okeeffe, *Acta Crystallogr., Sect. B-Struct. Science* **1991**, *47*, 192.
[37] K. Brandenburg, *Diamond*, v3.1a, *Crystal Impact GbR*, Bonn, Germany, **2005**.
[38] G. Kotuem, *Reflectance Spectroscopy*, Springer-Verlag, New York, **1969**.
[39] W. W. Wendlandt, H. G. Hecht, *Reflectance Spectroscopy*, Interscience Publishers, New York, **1966**.
[40] R. Tank, O. Jepsen, A. Burkhardt, O. K. Andersen, *TB-LMTO-ASA*, v4.7, Max-Plank-Institut für Festkörperforschung, Stuttgart, Germany, **1995**.
[41] O. K. Anderson, O. Jepson, *Solid State Commun.* **1971**, *9*, 1763.
[42] P. E. Blochl, O. Jepsen, O. K. Andersen, *Phys. Rev. B* **1994**, *49*, 16223.

Received: April 5, 2011
Published Online: August 22, 2011

